crystals

MDPI

Article

Cathodoluminescence of Diamond: Features of Visualization

Evgeny Vasilev [1,*], Dmitry Zedgenizov [2], Dmitry Zamyatin [2], Igor Klepikov [3] and Anton Antonov [4]

[1] Saint-Petersburg Mining University, 199106 Saint-Petersburg, Russia
[2] Zavaritsky Institute of Geology and Geochemistry, 620016 Ekaterinburg, Russia; zedgenizov@igg.uran.ru (D.Z.); zamyatin@igg.uran.ru (D.Z.)
[3] Saint-Petersburg State University, 199034 Saint-Petersburg, Russia; klepikov_igor@mail.ru
[4] Russian Geological Research Institute, 199106 Saint-Petersburg, Russia; anton_antonov@vsegei.ru
* Correspondence: Vasilev_EA@pers.spmi.ru

Abstract: Zonal and sectorial heterogeneities in natural diamonds provide information on the growth conditions and post-growth changes. Cathodoluminescence (CL) microscopy revealed these heterogeneities in a very detailed manner with high spatial resolution. In this study, factors affecting the CL images of two natural diamonds were analyzed and the results of cathodoluminescence studies in steady-state (SS-CL) and scanning modes were compared. SS-CL was observed using an optical microscope, and scanning mode was evaluated via SEM (SEM-CL). It was demonstrated that the relative brightness of the <111> and <100> growth sectors in diamond crystals depends on the nature of defects in them and on the method of image detection (steady-state/scanning versus color/panchromatic). The differences between SS-CL and SEM-CL images can be attributed to the kinetics of luminescence and spectral sensitivity of the detectors. It was established that the nature of lattice defects around small inclusions can be changed (e.g., the intensity of blue luminescence from nitrogen-vacancy defects (N_3V) decreases due to their transformation into nitrogen–hydrogen defects (N_3VH). The hydrogen disproportion between the sectors is caused by different growth mechanisms. Hydrogen atoms in the diamond matrix can affect the kinetics of transformation of the defects by transforming a part of N_3V to N_3VH.

Keywords: diamond; cathodoluminescence; FTIR; nitrogen; hydrogen

Citation: Vasilev, E.; Zedgenizov, D.; Zamyatin, D.; Klepikov, I.; Antonov, A. Cathodoluminescence of Diamond: Features of Visualization. *Crystals* **2021**, *11*, 1522. https://doi.org/10.3390/cryst11121522

Academic Editor: Juan Luis Nieves Gómez

Received: 9 November 2021
Accepted: 4 December 2021
Published: 6 December 2021

1. Introduction

Diamond is a crucial mineral for studying the subcontinental lithospheric mantle and sublithospheric horizons [1–3]. Diamond crystals record information about their growth conditions and later processes such as deformation by retaining chemical (from uncompromised inclusions) and time–temperature (nitrogen aggregation state) [4–8]. Internal features reveal the complexity of the growth processes of diamonds. The features are visualized via photoluminescence (PL), Fourier transform infrared absorption (FTIR), anomalous birefringence, and cathodoluminescence (CL). CL microscopy provides the most sensitive method for visualizing inhomogeneities in crystals with high resolution and contrast [9,10]. In diamonds, CL reveals zonal and sectorial growth heterogeneities [11–13], plastic deformation, and mechanical twinning layers [14,15] as well as irradiation-induced features [16]. More than 300 defects of crystal structure are known in diamond [17]; these appear and transform at all stages of crystal growth [18,19]. These defects are either CL active or they can interact with CL active defects, as such, they can decrease or increase the intensity of the corresponding luminescence systems. The CL spectra of most natural crystals contain a broad structureless band (*A-band*) with a maximum position spaced from 415 to 445 nm [20]. The nature of this system is unclear; evidently, it is related to dislocations and partial sp^2 hybridization [21]. Through defect levels with sp^2 hybridization, electron-hole pair recombination occurs, which manifests itself as the CL *A-band*. This process competes with the recombination of free (*N9* system) and bound (*N10* system) excitons [22]. In crystals with a more perfect structure, the intensity of the *N9* and *N10* systems is high and the intensity of

the *A-band* is low [23]. The CL recombination *A-band* is superimposed on the intracenter luminescence of the neutral vacancy, *V*(*GR1*), nitrogen vacancy, *NV* (575 nm), N_2V (*H3*), N_3V *(N3)*, N_4V_2 *(H4)* centers, and the broad structureless band of *B'* centers (platelets) [24]. The mechanisms of energy transfer to the PL centers during electron excitation in diamond have been poorly investigated [25,26]. The apparent zoning of crystals is mostly caused by nonuniform distribution of the *A-band* intensity as well as the *N3* and *H3* systems [27]. The concentration of *N3* and *H3* defects is limited by the nitrogen content in the form of N_2 (*A*) [28] and N_4V (*B*) [29] defects. The *N3* defect arises during *A*→*B* transformation, and *H3* occurs as a result of plastic deformation and irradiation. N_3VH is the common defect in diamond [30]. Notably, four impurity atoms replace four carbon atoms in the model; therefore, the model corresponds to the formula N_3H. The defect is not active in luminescence, but it appears in the FTIR absorption spectra at 3107 cm^{-1}. The nature of its interaction with other defects has not yet been documented. The intracenter luminescence intensity of the *N3* and *H3* systems depends on the concentration of luminescence centers, quenching centers, and perfection of the structure. Because of the complex nature of CL, features of the obtained images depend on many factors. In most studies, CL images of diamond crystals are demonstrated as being complex, without interpretation of their origin. Therefore, the explanation of the causes of CL inhomogeneities in crystals is an valuable, important, and interesting task. The study of causes of CL will increase the genetic information derived from the study of diamond crystals. Herein, we study the nature of some detectable CL heterogeneities in diamond crystals and investigate the influence of the detection method on the features of the obtained images.

2. Materials and Methods

2.1. Materials

This research was conducted using mixed-habit crystals with synchronous growth sectors of {111} and {100} faces. The sectors have the same thermal history but different sets of impurities and dislocation density [2,31–33]. The complex structure of the crystals does not often manifest in the diamond shape and can revealed by the study of polished plates [2]. In plates, the growth zones of the {111} and {100} faces can be clearly seen as sectors of the same direction. The study of these crystals revealed regularities in the formation and transformation of defects as a result of natural processes such as the natural annealing of a crystal with different sets of impurity sectors. Previously, the study of these crystals allowed [34] to draw conclusions on the different kinetics of defect transformation in the <111> and <100> sectors. However, the reason for the difference in the kinetics of defect formation in different growth sectors remains unclear.

In this study, internal heterogeneities of diamond crystals with synchronous <100> and <111> growth sectors from the Krasnovishersky placer region of the Urals were investigated [35]. The (100) plates were cut out of the centers of the crystals and polished. The orientation of the samples for cutting was conducted by morphological features. Square pits on a crystal surface clearly revealed L4 axes. After cutting, the <111> sectors were identified by layer-by-layer line zoning and the <100> sectors had curvilinear zoning [2]. The plate sizes of the crystals were 4.3 × 3.5 × 0.4 mm (sample 615-66) and 6.5 × 6.5 × 0.6 mm (sample 123-76).

2.2. Methods

Panchromatic CL images were acquired using a SEM CamScan MX2500S coupled with a QLI/QUA2 detector at an acceleration voltage of 12 kV and beam current of 5–7 nA. The plates were coated with sputtered gold. Color steady-state CL (SS-CL) images were obtained on an Mk5 (CITL) using a Ci Eclipse (Nikon, Tokyo, Japan) microscope at an accelerating voltage ranging from 12 to 20 kV at low vacuum without applying conductive sputtering. CL spectra were recorded at room temperature on a SEM JSM6390LV (Jeol, Tokyo, Japan) with an H-CLUE iHR500 system (Horiba, Tokyo, Japan) at an accelerating voltage of 10 KV with carbon coating. The luminescence in the SEM sample chamber was collected using a retractable parabolic mirror. The spectra were recorded using a

monochromator with a focal length of 500 mm and a grating of 150 g/mm, with a Synapse-Plus CCD-detector in the range of 200–800 nm at a spectral resolution of 0.9 nm. Spectral mapping was performed in the range of 300–550 nm.

PL images were obtained using a Leica M 205 binocular microscope with 405 nm laser excitation through a 450 nm edge light filter. Excitation at 405 nm was selected because it excited the main blue PL system *N3* with the zero-phonone line at 415 nm. An edge filter at 450 nm was used for laser line blocking and some reducing of the blue PL. The PL study allows for the visualization of the internal heterogeneities in the crystal quickly and without sample preparation, but a significant disadvantage of this method is its low contrast. Because PL is excited throughout the crystal volume, zones with different PL characteristics overlap and are blurred.

To determine the concentration of the main nitrogen defects, *A* (N_2) [28] and *B* (N_4V) [29], the FTIR absorption spectra were recorded. Absorption coefficients of the platelet B′ [36], peak ($a_{B'}$) position of maximum ($\nu_{B'}$) in the range 1360–1380 cm^{-1}, and the absorption band at 3107 cm^{-1} (a_{3107}) of N_3VH [30] defects were determined. FTIR spectra were obtained using a Vertex-70 spectrometer with a Hyperion2000 microscope in mapping mode at a resolution of 2 cm^{-1} with an aperture of 100 μm and a map step interval of 100 μm. The concentrations were calculated using known relations [28,29]. When interpreting FTIR data, the nonlinear nature of the dependence of the fraction of *B* defects (N_{BS}) on the total nitrogen concentration, N_{tot}, and overlapping sectors of zones [37] should be considered. Therefore, quantitative analysis of FTIR data should be conducted on plates of limited thickness or by profiles passing through homogeneous regions in the volume. Absorption spectroscopy has a lower spatial resolution than CL because it is limited by the thickness of the plate. Therefore, the distribution maps of the FTIR data do not have clear boundaries, unlike CL images.

3. Results

Sample 615-66 had a contrasting zonal-sectoral structure. Sectors of <111> growth were brighter than the <100> sectors in the SEM-CL image, and vice versa in the SS-CL image. The sample is interesting because of the presence of isometric dark spots in the <100> sectors in the panchromatic CL image (Figure 1). These spots were 35 μm in diameter and were not detected in the <111> sectors. Sub-micron-sized inclusions were detected in the region of the spots in the dark-field image. These inclusions were associated with rosette-shaped cracks that enhanced their contrast in the dark-field optical image (Figure 1b). In the PL image, the <100> sectors had weak contrast at an excitation of 405 nm. Similar features in mixed-habit crystals were shown in [38], and a decrease in the CL brightness around the inclusions was occasionally observed [39,40].

In the SS-CL image, the dark spots had weak contrast and a yellowish color. Figure 1h–j shows the SS-CL images of the area highlighted in (e) by the intensity of the blue (b), green (c), and red (d) RGB encoding channels, indicating that the dark regions corresponded to the attenuation of the blue luminescence. Additionally, the spots remained weakly contrasting in this imaging mode. Due to the weak contrast, these areas were not detected in the normal SS-CL observation or were mistaken for artefacts.

The CL spectra revealed differences in the main volume of the <100> and <111> sectors as well as dark spots in the <100> sectors. Figure 2c shows an area of the CL image in which the mapping was performed as well as the spectra of the contrasting regions (Figure 2a) and main CL features (Figure 2b). The CL intensity ratio map at wavelengths of 400 and 450 nm (Figure 2d) showed that the maximum intensity shifted to the short-wavelength region in the dark spots. The *A-band* dominated in the spectrum of sector <111>, whereas its intensity was two times lower in the <100> sector. In the spectrum from the <100> sector, the *N3* system with the zero-phonone line at 415 nm was detected. Its intensity at the phonon wing maximum was 30% that of the *A-band*. However, the *N3* system was not detected in the dark spots. In the spectrum from the <111> sector, the intensity of the structureless band with a maximum close to 530 nm was high, which was attributed to

the CL from platelets [41]. This luminescence occasionally makes it possible to observe individual platelets exceeding 0.7–1 μm in the CL images in SS-CL mode.

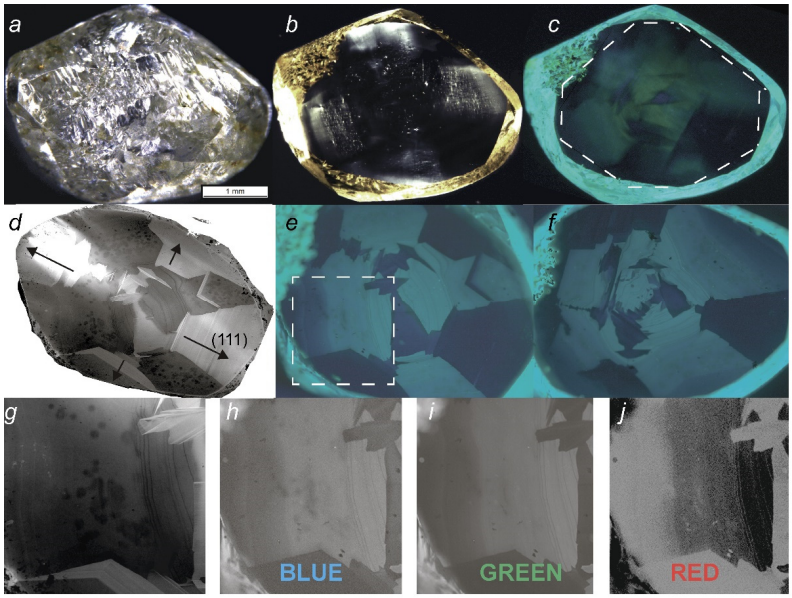

Figure 1. Images of crystal 615-66. (**a**) General view; (**b**) the plate in transmitted light (dark field); (**c**) photoluminescence (PL) at an excitation of 405 nm; (**d**) panchromatic luminescence SEM-CL; (**e**,**f**) color SS-CL on both sides of the plate. Images of the area highlighted in (**e**) panchromatic SEM-CL (**g**) and by RGB coding channels: (**h**) blue, (**i**) green, and (**j**) red. Arrows on (**d**) show the direction of the <111> sectors. The white area (*w*) on (**d**) is an artifact due to surface charging. The dotted line on (**c**) corresponds to boundaries of the FTIR maps in Figure 2.

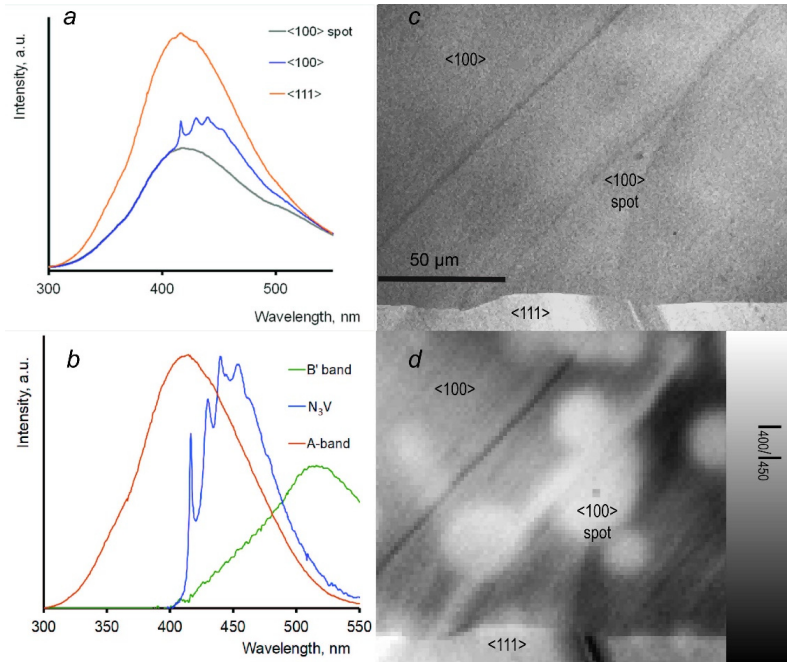

Figure 2. CL spectra of crystal 615–66 and images of their analysis location. (**a**) SS-SEM CL spectra in the <100> and <111> sectors and dark spots in the <100> sectors at room temperature; (**b**) main components of the SS-SEM CL spectra. Comparison of the panchromatic image (**c**) of the region with dark CL spots and the synthesized image with the ratio of the CL intensities at 400 and 450 nm I_{400}/I_{450} (**d**).

Additionally, the complex internal structure of the crystal was evident in the FTIR spectral maps. The pattern of disproportionality of the a_{3107} in the <100> and <111> sectors was confirmed using an example of the crystal.

Figure 3 shows that the <111> sectors had higher N_{tot} and $a_{B'}$ as well as lower a_{3107} compared with the <100> sectors. Platelets were observed only in regions with maximum N content and minimum values of a_{3107}. The inverse relationship between $a_{B'}$ and a_{3107} was noted earlier [31,38,42]. As shown in Figure 3, the distribution contours of $a_{B'}$ did not exactly repeat the contours of a_{3107}. The N_{BS} value in this crystal was less than 5%. In crystals of mixed-habit, the concentration of the N_3VH center in synchronous zones of the <100> sectors was higher than that in the <111> sectors [33]. The distribution of the defects within individual sectors was uniform, which is typical for mixed-habit crystals [34].

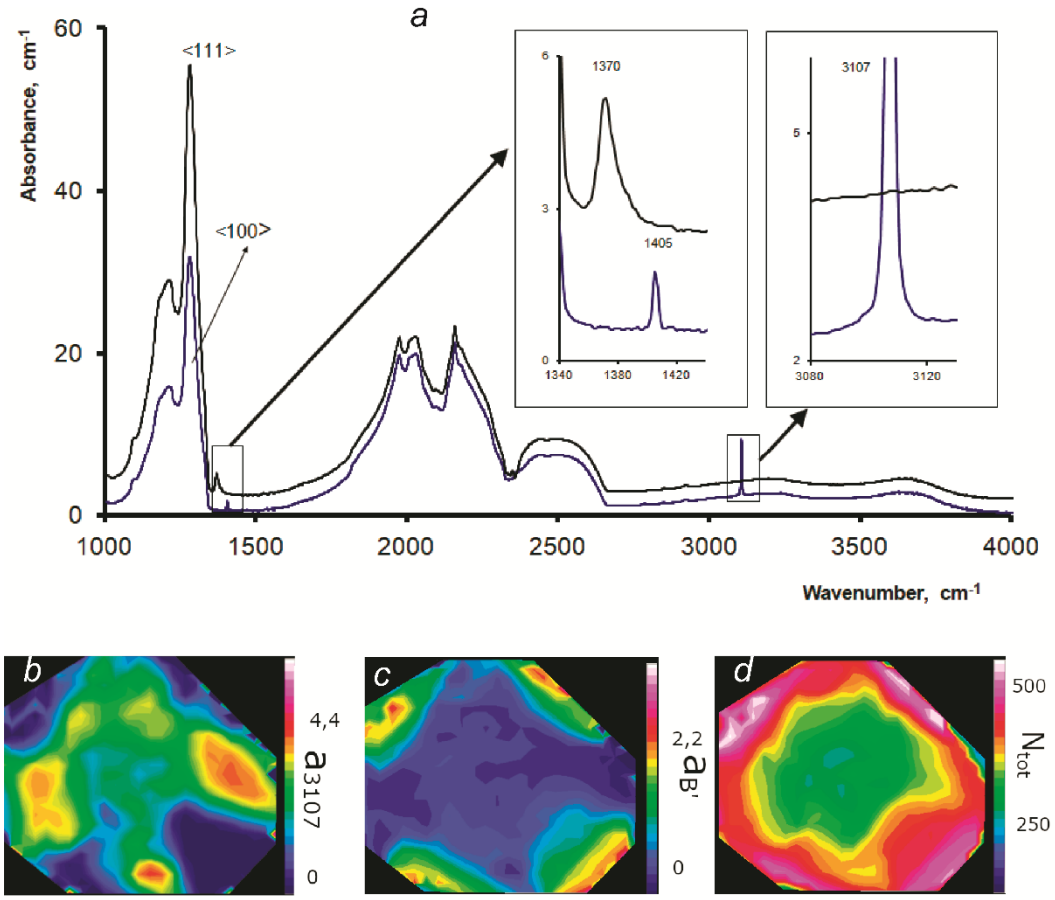

Figure 3. FTIR spectra of synchronous zones of the <100> and <111> sectors in crystal 615-66 (**a**) and distribution maps of N_{tot} (**b**); a_{3107} (**c**); a_{B2} (**d**). The captions in maps show the minimum and maximum values of parameters.

In another mixed-habit crystal (123-76), there was limited contrast between the <100> and <111> sectors in the SS-CL and SEM-CL images (Figure 4a,b). In addition, there were no discrepancies between the SS-CL and SEM-CL images. The growth zonation was strongly exhibited in the <100> sectors; the <111> sectors were almost homogeneous in CL. The <100> sectors in this crystal were saturated with microinclusions, which is the general rule. The sizes of the inclusions were smaller compared to those in sample 615-66, all were smaller than one μm. The inclusions were not visible in the CL images. All FTIR data parameters had a sectorial distribution (Figure 4d–g).

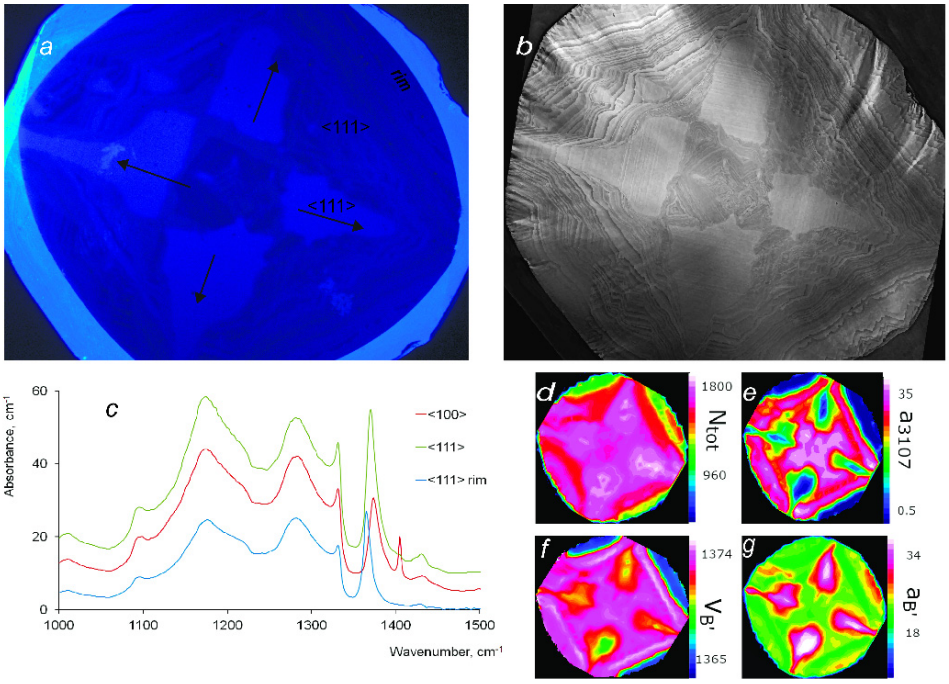

Figure 4. Images of crystal 123-76. (**a**) Color luminescence SS-CL; (**b**) Panchromatic luminescence SEM-CL; (**c**) FTIR spectra of the synchronous zones of the <100> and <111> sectors as well as outer zone marked in (**a**) as "*rim*"; Distribution maps, N_{tot} (**d**); a_{3107} (**e**); $a_{B'}$ (**f**); $v_{B'}$ (**g**). The arrows in (**a**) show the <111> directions. A bright rim in (**a**) is the crystal's surface, highlighted by reflected luminescence light.

The outer zone was distinct in the FTIR data maps, and there were growth layers of {111} faces in this zone, covering the inner <100> sectors. In this crystal, N_{BS} reached 70%. The N_{tot} in the synchronous zones of the <111> and <100> sectors was 1500 and 1300 ppm, whereas a_{3107} were 0.6 and 35 cm, respectively (Figure 4c). The concentration of *N3* centers in <111> and <100> sectors differed slightly. There were no significant differences in spectral composition and CL intensity between the sectors. Outer parts of the crystal had octahedral zoning in which nitrogen concentration decreased to 800 ppm and a_{3107} was less than 0.4 cm^{-1}.

4. Discussion

4.1. CL Features in SS-CL and SEM-CL Modes

According to the Kanaya–Okayama relation [43], the electron penetration depths in diamond at energies of 20 and 10 KeV were 2.5 and 1 µm, respectively. The CL excitation volume was comparable to the electron penetration depth; therefore, at 10 KeV, the size of the detectable SEM-CL inhomogeneities was approximately 2 µm, which is above the diffraction limit of optical microscopy. The CL locality in scanning mode was determined by the area of CL generation and the diffusion length of the charge carriers. The diffusion length of carriers in the most perfect nitrogen-free crystals is one µm and significantly lower in nitrogen-containing crystals [44].

The advantages of SS-CL optical microscopy are the observation of natural CL colors, weak surface charging effects, and potentially high resolution. Contrast is higher in the SEM-CL mode because of high electron flux density. However, the optimal detection of inhomogeneities depends on the kinetic characteristics of the luminescence because scanning highlights systems with short excitation and attenuation times, whereas steady-state mode highlights systems with long afterglow. Previously, in the study of low-nitrogen crystals, it was established that during pulsed excitation by an electron beam, the *N3* system has an attenuation time of 30–50 ns, and the *A-band* had an attenuation time of

8–9 ms [27]. Therefore, in the scanning mode, a fast detector registers *N3* luminescence. The video camera of an optical microscope operates in the SS-CL mode and has long exposure time. Therefore, the intensity of systems with long attenuation time increased. Notably, the probability of radiation-free transitions increased with increasing nitrogen concentration; thus, the attenuation time of the *N3* system decreased. Therefore, in addition to the spectral sensitivity of the detectors, the kinetic parameters of excitation and the luminescence detection method affect the character of the CL intensity distribution. Fast-decay systems appear stronger in the scanning mode, and the contribution of systems with long decay time increased in the steady-state mode.

In the steady-state mode, reflected light illuminates cracks, inclusions, and surface inhomogeneities and reduces the image contrast. Thus, the brightness of different zones is determined, on one hand, by the admixture composition of diamond, and on the other hand, by the conditions of image acquisition: spectral sensitivity of the photodetector and scanning speed.

4.2. FTIR Heterogeneity Analysis

It is proposed that the transformation of *A* defects proceeds through intermediate nitrogen-vacancy centers. Calculations showed that the mobility of nitrogen-vacancy centers is significantly higher than that of nitrogen in *C* and *A* defects [36,45]. There are various models (1–5) for the formation of *B* centers, in which nitrogen-vacancy defects are considered as intermediate defects [36,45].

$$A(\mathrm{N_2}) + (I + V) \rightarrow H3(\mathrm{N_2}V) + I;\ \mathrm{n}I \rightarrow I_\mathrm{n}(B');\ H3(\mathrm{N_2}V) + A(\mathrm{N_2}) \rightarrow B\ (\mathrm{N_4}V) \quad (1)$$

$$\begin{gathered} A(\mathrm{N_2}) \rightarrow 2C(\mathrm{N});\ C + A(\mathrm{N_2}) \rightarrow N3(\mathrm{N_3}V) + \mathrm{I};\ \mathrm{n}I \rightarrow I_\mathrm{n}(B');\\ N3(\mathrm{N_3}V) + C(\mathrm{N}) \rightarrow B\ (\mathrm{N_4}V) \end{gathered} \quad (2)$$

$$I_\mathrm{n} + (I + V) \rightarrow I_{\mathrm{n}+1} + V;\ A(\mathrm{N_2}) + V \rightarrow H3(\mathrm{N_2}V);\ H3(\mathrm{N_2}V) + A(\mathrm{N_2}) \rightarrow B\ (\mathrm{N_4}V) \quad (3)$$

$$\begin{gathered} I_\mathrm{n} + (I + V) \rightarrow I_{\mathrm{n}+1}(B') + V;\ A(\mathrm{N_2}) \rightarrow 2C(\mathrm{N});\ C(\mathrm{N}) + V \rightarrow \mathrm{N}V;\\ A(\mathrm{N_2}) + \mathrm{N}V \rightarrow N3(\mathrm{N_3}V);\ N3(\mathrm{N_3}V) + C(\mathrm{N}) \rightarrow B\ (\mathrm{N_4}V) \end{gathered} \quad (4)$$

$$\begin{gathered} A(\mathrm{N_2}) \rightarrow 2C(\mathrm{N});\ A(\mathrm{N_2}) + (I{+}V) \rightarrow H3(\mathrm{N_2}V);\\ H3(\mathrm{N_2}V) + C(\mathrm{N}) \rightarrow N3(\mathrm{N_3}V){:}\ N3(\mathrm{N_3}V) + C(\mathrm{N}) \rightarrow B\ (\mathrm{N_4}V) \end{gathered} \quad (5)$$

The formation of *B* defects results in the formation of interstitial carbon atoms *I*, which then form B′ defects—platelets (I_n). In a diamond matrix with dislocations and inclusions, most of the interstitial atoms that form at this stage do not transform into platelets; the carbon atoms flow into dislocations and microinclusions. Therefore, the beginning of the formation of platelets in the <100> sectors was delayed compared to the <111> sectors. Due to the low concentration of interstitial atoms, the concentration of platelets in the <100> sectors was lower than that in the <111> sectors, but had a larger size. This peculiarity corresponds to the formation of platelets through solid solution decomposition. There seems to be no direct causal relationship in the inverse relationship between a_{3107} and $a_{B'}$. The inverse dependence results from various general regularities: (1) lower hydrogen concentration in the <111> sectors than in the <100> sectors; (2) high N_tot concentration in the <111> sectors; and (3) high dislocation and microinclusions density in the sectors <100>. The dependence of a_{B2} on the nitrogen concentration in form *B* (N_B) is linear [36], whereas the dependence of N_B on N_tot is quadratic, which follows from the kinetic equation [29]. Therefore, a difference of 10–20% N_tot was accompanied by a difference of 30–40% in $a_{B'}$.

According to the existing models, platelets arise as a drain of interstitial atoms. What reasons alter the kinetics of transformed interstitial carbon atoms in <100> sectors? Howell et al. [34] suggested that interstitial carbon atoms flow to disc-crack-like defects, a phenomenon found in cuboid diamonds. Not only microinclusions, but also dislocations can be a possible drain for very mobile interstitial carbon atoms, which are characteristic for <100> sectors [34,46]. The high density of dislocations and microinclusions in the sectors <100> is caused by the normal mechanism of their growth. The presence of an alternative

drain for interstitial atoms significantly affects the formation of platelets. The formation of platelets is described by the kinetics of the decay of the solid solution of interstitial carbon atoms in the diamond matrix [47]. The number of interstitial carbon atoms formed is proportional to the $A \rightarrow B$ reaction rate. Additionally, when the interstitial carbon atoms have an outlet, the concentration of the formed platelets decreases sharply compared to the matrix in which there is no alternate outlet for the interstitial carbon atoms. Two types of diamond matrix with identical thermal history are <111> and <100> sectors in mixed-habit crystals. The hydrogen disproportion between the <111> and <100> sectors is because of their different growth mechanism. Diamond in the <111> sectors grows via a layer-by-layer tangential mechanism and via a normal mechanism in the <100> sectors. The normal or tangential growth mechanism determines the features of morphology, impurity, and defect composition of crystals. The <100> sectors capture more hydrogen and submicron inclusions, which determines the type and characteristics of the PL and FTIR spectra.

4.3. Analysis of CL Heterogeneities

In mixed-habit crystals, the CL of the <100> sectors can either be brighter or weaker than that of the <111> sectors under identical observational conditions [31]. In most studies, the CL of the <100> sectors is brighter than that of the <111> sectors [38]. In <111> sectors of crystal 615-66, the *A-band* intensity was twice as high as that in the <100> sectors. In the <100> sectors, the intensity of the *N3* system was high. The intensity of the *N3* system locally decreased around the inclusions, but the intensity of the *A-band* did not change. The decrease in intensity can be attributed to the decrease in the concentration of luminescence centers, quenching by other defects, and general decrease in the perfection of the crystal structure. The concentration of defects can be detected via absorption spectroscopy. However, the detection of absorption spectra in 30 μm areas requires appropriate sample thickness. The phenomenon of decreasing *N3* concentration in the areas of diamond crystal with reduced *N3* system intensity in the SS-SEM CL mode has been previously described [48]. A high concentration of N_3VH was observed in the region without *N3* defects (according to the absorption data). The inverse relationship between the concentrations *of N3* and N_3VH could be attributed to the transformation of the former into the latter during hydrogen atom capture. By considering the phases in the inclusions as a local source of hydrogen, we can write down the equation of $N3 + H \rightarrow N_3VH$ transformation. This equation explains the decrease in the *N3* system intensity in the inclusion region. As shown above, the defect concentration in N_3VH was not related to the degree of nitrogen aggregation from $A \rightarrow B$. In neighboring <100> and <111> sectors, the concentration of N_3VH can differ by a factor of 50, but there were no differences in the degree of aggregation of nitrogen between the sectors. Thus, hydrogen atoms transform *N3* centers into N_3VH. Consequently, *N3* defects are not the main intermediate center in the $A \rightarrow B$ transformation and form only as one of the side variants of the defect transformation. In the <100> sectors, hydrogen transforms *N3* defects into the N_3VH form, which explains the low intensity of *N3* luminescence.

4.4. Evolution of Defect Set during Natural Annealing

Comparison of crystals shows that the differences between defect distribution in the <111> and <100> sectors changed during natural annealing and were the highest at the first stage of defect transformation $A \rightarrow B$ in crystal 615-66. According to modern concepts, nitrogen atoms are incorporated in the diamond matrix in the form of *C* defects. Thereafter, the *C* defects are transformed into *A* defects. The temperature and time of natural annealing of most crystals are such that all *C* defects transform into form *A*. The next stage of transformation $A \rightarrow B$ is achieved in diamond crystals to different degrees. During this stage, concentration of N_3VH increases [49]. In crystals of mixed-habit, the effects influencing transformation of defects have been revealed. The first effect is the influence of the rate of platelet formation; the second effect is the transformation of $N3 \rightarrow N_3VH$. During the first stage of natural annealing, there are no platelets in <100> sectors, but they are present in

<111> sectors. This difference is greatest in crystals with low aggregation of $A \rightarrow B$ defects, and decreases during natural annealing. Because the formation of platelets occurs via solid solution decomposition, their concentration is low during the first stage of annealing. During further transformation of $A \rightarrow B$ defects, the concentration of platelets does not change, but they increase in size. Therefore, in the <100> pyramids, the concentration of platelets is low but their size is large, and this pattern does not change during further annealing. Therefore, the <100> and <111> sectors differ in the green luminescence intensity of the *B′* defects. The second effect is explained by the fact that the hydrogen atoms withdraw a part of the intermediate defects, *N3,* from the transformation chain $A \rightarrow B$ and transform them into N_3VH. During prolonged annealing, all hydrogen atoms transform into N_3VH, and the concentration of *N3* defects in the <100> and <111> sectors is equalized. Thus, the differences between the <100> and <111> sectors are greatest during crystal growth, but diminished during prolonged post-growth natural annealing.

5. Conclusions

In diamond crystals, the relative brightness of the CL of growth sectors <111> and <100> depends on the nature of defects in them and the mode of image registration (stationary/scanning and color/panchromatic). The difference between the SS-CL and SEM-CL images is attributed to the set of point defects, difference in the kinetics and spectra of their luminescence as well as the spectral sensitivity of the detectors. Peculiarities of the luminescence distribution between the <111> and <100> growth sectors are associated with different hydrogen concentrations, dislocation density, and concentration of inclusions. Hydrogen atoms in the diamond matrix can change the kinetics of defect transformation by conversion of *N3* (N_3V) into N_3VH defects. A local change in the set of defects in the crystal structure can occur around inclusions, which are highly likely to be a local source of hydrogen. The study of the internal structure of diamond crystals allows for the reconstruction of their growth conditions and reveals the processes involved in the transformation of the crystal structure defects.

Author Contributions: Conceptualization and methodology, FTIR data acquisition, E.V.; Sample preparation, PL visualization, I.K.; CL visualization, A.A., D.Z. (Dmitry Zamyatin), D.Z. (Dmitry Zedgenizov); CL spectra analysis, D.Z. (Dmitry Zamyatin); Writing—original draft preparation, E.V.; Writing—reviewing and editing I.K., D.Z. (Dmitry Zamyatin), D.Z. (Dmitry Zedgenizov), A.A.; Project administration, D.Z. (Dmitry Zedgenizov). All authors have read and agreed to the published version of the manuscript.

Funding: The authors gratefully acknowledge the financial support from the Russian Science Foundation, grant number 21-77-20026.

Institutional Review Board Statement: Not applicable.

Informed Consent Statement: Not applicable.

Data Availability Statement: Not applicable.

Acknowledgments: The re-equipment and comprehensive development of the «Geoanalitik» shared research facilities of the IGG UB RAS is supported by a grant from the Ministry of Science and Higher Education of the Russian Federation for 2021–2023 (Agreement No. 075-15-2021-680). The authors are grateful to G.B. Mikhalevsky for help with the CL spectra measurements.

Conflicts of Interest: The authors declare no conflict of interest.

References

1. Gurney, J.J.; Helmstaedt, H.H.; Le Roex, A.P.; Nowicki, T.E.; Richardson, S.H.; Westerlund, K.J. Diamonds: Crustal distribution and formation processes in time and space and an integrated deposit model. *Econ. Geol.* **2005**, *100*, 143–177. [CrossRef]
2. Smit, K.V.; Shirey, S.B.; Stern, R.A.; Steele, A.; Wang, W. Diamond growth from C-H-N-O fluids in the lithosphere: Evidence from CH4 micro-inclusions and 13C-15N-N content in Zimbabwe mixed-habit diamonds. *Lithos* **2016**, *265*, 68–81. [CrossRef]

3. Shirey, S.B.; Smit, K.V.; Pearson, G.D.; Walter, M.J.; Aulbach, S.; Brenker, F.E.; Bureau, H.; Burnham, A.D.; Cartigny, P.; Chacko, T.; et al. Diamonds and the Mantle Geodynamics of Carbon. In *Deep Carbon: Past to Present*; Orcutt, B., Daniel, I., Dasgupta, R., Eds.; Cambridge University Press: Cambridge, UK, 2019; pp. 89–128, ISBN 9781108677950.
4. Spetsius, Z.V.; Bogush, I.N.; Kovalchuk, O.E. FTIR mapping of diamond plates of eclogitic and peridtotitc xenoliths from the Nyurinskaya pipe, Yakutia: Genetic implications. *Russ. Geol. Geophys.* **2015**, *56*, 344–353. [CrossRef]
5. Stepanov, A.S.; Shatsky, V.S.; Zedgenizov, D.A.; Sobolev, N.V. Causes of variations in morphology and impurities of diamonds from the Udachnaya Pipe eclogite. *Russ. Geol. Geophys.* **2007**, *48*, 758–769. [CrossRef]
6. Bruce, L.F.; Kopylova, M.G.; Longo, M.; Ryder, J.; Dobrzhinetskaya, L.F. Luminescence of diamonds from metamorphic rocks. *Am. Mineral.* **2011**, *1*, 14–22. [CrossRef]
7. Howell, D. Strain-induced birefringence in natural diamond: A review. *Eur. J. Mineral.* **2012**, *4*, 575–585. [CrossRef]
8. Wiggers de Vries, D.F.; Bulanova, G.P.; De Corte, K.; Pearson, D.G.; Craven, J.A.; Davies, G.R. Micron–scale coupled carbon isotope and nitrogen abundance variations in diamonds: Evidence for episodic diamond formation beneath the Siberian Craton. *Geochim. Cosmochim. Acta* **2013**, *100*, 176–199. [CrossRef]
9. Pagel, M.; Barbin, V.; Blanc, P.; Ohnenstetter, D. Cathodoluminescence in Geosciences: An Introduction. In *Cathodoluminescence in Geosciences*; Pagel, M., Barbin, V., Blanc, P., Ohnenstetter, D., Eds.; Springer: Berlin/Heidelberg, Germany, 2000; ISBN 978-3-662-04086-7.
10. Frelinger, S.N.; Ledvina, M.D.; Kyle, J.R.; Zhao, D. Scanning electron microscopy cathodoluminescence of quartz: Principles, techniques and applications in ore geology. *Ore Geol. Rev.* **2015**, *65*, 840–852. [CrossRef]
11. Hanley, P.L.; Kiflawi, I.; Lang, A.R. On topographically identifiable sources of cathodoluminescence in natural diamonds. *Philos. Trans. R. Soc.* **1977**, *A284*, 329–368. [CrossRef]
12. Bulanova, G.P.; Pearson, D.G.; Hauri, E.H.; Griffin, B. Carbon and nitrogen isotope systematics within a sector-growth diamond from the Mir kimberlite, Yakutia. *Chem. Geol.* **2002**, *188*, 105–123. [CrossRef]
13. Titkov, S.; Saparin, G.; Obyden, S. Evolution of growth sectors in natural diamond crystals as revealed by cathodoluminescence topography. *Geol. Ore Depos.* **2002**, *44*, 350–360.
14. Gaillou, E.; Post, J.E.; Rose, T.R.; Butler, J.E. Cathodoluminescence of Natural, Plastically Deformed Pink Diamonds. *Microsc. Microanal.* **2012**, *18*, 1292–1302. [CrossRef] [PubMed]
15. Gaillou, E.; Post, J.E.; Bassim, N.; Zaitsev, A.M.; Rose, T.R.; Fries, M.D.; Stroud, R.M.; Steele, A.; Butler, J.E. Spectroscopic and microscopic characterization of color lamellae in natural pink diamonds. *Diam. Relat. Mater.* **2010**, *19*, 1207–1220. [CrossRef]
16. Nasdala, L.; Grambole, D.; Wildner, M.; Gigler, A.; Hainschwang, T.; Zaitsev, A.; Harris, J.W.; Milledge, J.; Schulze, D.J.; Hofmeister, W.; et al. Radio-colouration of diamond: A spectroscopic study. *Contrib. Mineral. Petrol.* **2013**, *5*, 843–861. [CrossRef]
17. Dishler, B. *Handbook of Spectral Lines in Diamond*; Springer: Berlin/Heidelberg, Germany, 2001; p. 467.
18. Boyd, S.R.; Mattey, D.P. ; Pillinger, C.T.; Milledge, H.J.; Mendelssohn, M.; Seal, M. Multiple growth events during diamond genesis: An integrated study of carbon and nitrogen isotopes and nitrogen aggregation state in coated stones. *Earth Planet Sci. Lett.* **1987**, *86*, 341–357. [CrossRef]
19. Dobrinets, I.A.; Vins, V.G.; Zaitsev, A.M. *HPHT—Treated Diamonds: Diamonds Forever*; Springer: Berlin/Heidelberg, Germany, 2013; p. 276.
20. Ruan, J.; Kobashi, K.; Choyke, W.J. On the "band A" emission and boron related luminescence in diamond. *App. Phys. Lett.* **1992**, *25*, 3138–3140. [CrossRef]
21. Takeuchi, D.; Watanabe, H.; Yamanaka, S.; Okushi, H.; Sawada, H.; Ichinose, H.; Sekiguchi, T.; Kajimura, K. Origin of band-A emission in diamond thin films. *Phys. Rev. B* **2001**, *63*, 245–328. [CrossRef]
22. Robins, L.H.; Farabaugh, E.N.; Feldman, A. Cathodoluminesce spectroscopy of free and bound excitons in chemical-vapor-deposited diamond. *Phys. Rev. B* **1993**, *19*, 14167–14181. [CrossRef]
23. Kawarada, H.; Tsutsumi, T.; Hirayama, H.; Yamaguchi, A. Dominant free—Exciton recombination radiation in chemical vapor deposited diamonds. *Appl. Phys. Lett.* **1994**, *4*, 451–453. [CrossRef]
24. Zaitsev, A.M. *Optical Properties of Diamond: Data Handbook*; Springer: Berlin/Heidelberg, Germany, 2001; p. 502.
25. Lipatov, E.I.; Genin, D.E.; Grigor'ev, D.; Tarasenko, V.F. Recombination Radiation in the Diamond. In *Luminescence—An Outlook on the Phenomena and their Applications*; Thirumalai, J., Ed.; Intech Publisher: London, UK, 2016; pp. 191–224, ISBN 978-953-51-2763-5.
26. Panzer, G.; Gaft, M.; Marfunin, A.S. Systems of interacting luminescence centers in natural diamonds: Laser-induced time-resolved and cathodoluminesce spectroscopy. In *Cathodoluminescence in Geosciences*; Pagel, M., Barbin, V., Blanc, P., Ohnenstetter, D., Eds.; Springer: Berlin/Heidelberg, Germany, 2000; pp. 359–371, ISBN 978-3-662-04086-7.
27. Lipatov, E.I.; Lisitsyn, V.M.; Oleshko, V.I.; Tarasenko, V.F. Spectral and kinetic characteristics of the pulsed cathodoluminescence of a natural IIA-type diamond. *Russ. Phys. J.* **2007**, *1*, 52–57. [CrossRef]
28. Boyd, S.R.; Kiflawi, I.; Woods, G.S. The relationship between infrared absorption and the A defect concentration in diamond. *Philos. Mag. B* **1994**, *69*, 1149–1153. [CrossRef]
29. Boyd, S.R.; Kiflawi, I.; Woods, G.S. Infrared absorption by the B nitrogen aggregate in diamond. *Philos. Mag. B* **1995**, *72*, 351–361. [CrossRef]
30. Goss, J.P.; Briddon, P.R.; Hill, V.; Jones, R.; Rayson, M.J. Identification of the structure of the 3107 cm^{-1} H-related defect in diamond. *J. Phys. Condens. Matter.* **2014**, *26*, 1–6. [CrossRef] [PubMed]

31. Rondeau, B.; Fritsch, E.; Guiraud, M.; Chalain, J.P.; Notari, F.E. Three historical "asteriated" hydrogen-rich diamonds: Growth history and sector-dependent impurity incorporation. *Diam. Relat. Mater.* **2004**, *13*, 1658–1673. [CrossRef]
32. Howell, D.; Griffin, W.L.; Pearson, N.J.; Powell, W.; Wieland, P.; O'Reilly, S.Y. Trace element partitioning in mixed-habit diamonds. *Chem. Geol.* **2013**, *355*, 134–143. [CrossRef]
33. Howell, D.; O'Neill, C.; Grant, K.J.; Griffin, W.L.; Pearson, N.J.; O'Reilly, S.Y. μ-FTIR mapping: Distribution of impurities in different types of diamond growth. *Diam. Relat. Mater.* **2012**, *29*, 29–36. [CrossRef]
34. Howell, D.; O'Neill, C.J.; Grant, K.J.; Griffin, W.L.; O'Reilly, S.Y.; Pearson, N.J.; Stern, R.A.; Stachel, T. Platelet development in cuboid diamonds: Insights from micro-FTIR mapping. *Contrib. Mineral. Petrol.* **2012**, *164*, 1011–1025. [CrossRef]
35. Klepikov, I.V.; Vasilev, E.A.; Antonov, A.V. The Defect-Impurity Composition of Diamond Crystals with <100> Growth Pyramids from Placers of the Krasnovishersk District, the Urals. *Geol. Ore Deposit.* **2020**, *8*, 743–753. [CrossRef]
36. Goss, J.P.; Coomer, B.J.; Jones, R.; Fall, C.; Briddon, P.; Öberg, S. Extended defects in diamond: The interstitial platelet. *Phys. Rev. B* **2003**, *67*, 165208. [CrossRef]
37. Kohn, S.C.; Speich, L.; Smith, C.B.; Bulanova, G.P. FTIR thermochronometry of natural diamonds: A closer look. *Litos* **2016**, *265*, 148–158. [CrossRef]
38. Howell, D.; Griffin, W.L.; Piazolo, S.A.; Say, J.M.; Stern, R.A.; Stachel, T.; Nasdala, L.; Rabeau, J.R.; Pearson, N.J.; O'Reilly, S.Y. A spectroscopic and carbon-isotope study of mixed-habit diamonds: Impurity characteristics and growth environment. *Am. Mineral.* **2013**, *98*, 66–77. [CrossRef]
39. Thomson, A.R.; Kohn, S.C.; Bulanova, G.P.; Smith, C.B.; Araujo, D.; EIMF; Walter, M.J. Origin of sub-lithospheric diamonds from the Juina-5 kimberlite (Brazil): Constraints from carbon isotopes and inclusion compositions. *Contrib. Mineral. Petrol.* **2014**, *168*, 1081–1088. [CrossRef]
40. Ragozin, A.L.; Zedgenizov, D.A.; Shatsky, V.S.; Kuper, K.E. Formation of mosaic diamonds from the Zarnitsa kimberlite. *Russ. Geol. Geophys.* **2018**, *5*, 486–498. [CrossRef]
41. Kiflawi, I.; Lang, A.R. Polarised infrared cathodoluminescence from platelet defects in natural diamonds. *Nature* **1977**, *1324*, 36–37. [CrossRef]
42. Zedgenizov, D.A.; Harte, B. Microscale variations of d13C and N content within a natural diamond with mixed-habit growth. *Chem. Geol.* **2004**, *205*, 169–175. [CrossRef]
43. Kanaya, K.; Okayama, S. Penetration and energy loss theory of electrons in solid targets. *J. Phys. D Appl. Phys.* **1972**, *5*, 43–58. [CrossRef]
44. Malinauskas, T.; Jarasiunas, K.; Ivakin, E.; Ralchenko, V.; Gontar, A.; Ivakhnenko, S. Optical evaluation of carrier lifetime and diffusion length in synthetic diamonds. *Diam. Relat. Mater.* **2008**, *7–10*, 1212–1215. [CrossRef]
45. Vins, V.G.; Eliseev, A.P. Effect of annealing at high pressures and temperatures on the defect-admixture structure of natural diamonds. *Inorg. Mater. Appl. Res.* **2010**, *4*, 303–310. [CrossRef]
46. Zedgenizov, D.; Harte, B.; Shatsky, V.S.; Politov, A.A.; Rylov, G.M.; Sobolev, N.V. Directional chemical variations in diamonds showing octahedral following cuboid growth. *Contrib. Mineral. Petrol.* **2006**, *151*, 45–57. [CrossRef]
47. Vasilyev, E.A.; Sofroneev, S.V. Zoning in diamonds from Mir kimberlite pipe: FTIR data. *Geol. Ore Deposit.* **2008**, *8*, 784–791. [CrossRef]
48. Vasilev, E.; Petrovsky, V.; Kozlov, A.; Antonov, A.; Kudriavtsev, A.; Orekhova, K. The story of one diamond: The heterogeneous distribution of the optical centres within a diamond crystal from the Ichetju placer, northern Urals. *Miner Mag.* **2019**, *4*, 515–522. [CrossRef]
49. Zedgenizov, D.A.; Kalinin, A.A.; Kalinina, V.V.; Palyanov, Y.N.; Shatsky, V.S. Nitrogen and hydrogen aggregation in natural octahedral and cuboid diamonds. *Geochem. J.* **2017**, *51*, 181–192. [CrossRef]